Magnetic Resonance Materials in Physics, Biology and Medicine
https://doi.org/10.1007/s10334-020-00863-3

RESEARCH ARTICLE

Characterization of hardware-related spatial distortions for IR-PETRA pulse sequence using a brain specific phantom

Sima Ahmadian[1] · Iraj Jabbari[1] · Seyed Mehdi Bagherimofidi[2] · Hamidreza Saligheh Rad[3,4]

Received: 31 December 2019 / Revised: 22 June 2020 / Accepted: 24 June 2020

Abstract

Objective Inversion recovery-pointwise encoding time reduction with radial acquisition (IR-PETRA) is an effective magnetic resonance (MR) pulse sequence in generating pseudo-CTs. The hardware-related spatial-distortion (HRSD) in MR images potentially deteriorates the accuracy of pseudo-CTs. Thus, we aimed at characterizing HRSD for IR-PETRA.

Materials and methods *gross*-$HRSD_{overall}$ (Euclidean-sum of *gross*-$HRSD_i$ ($i = x, y, z$)) for IR-PETRA was assessed using a brain-specific phantom for two MR scanners (1.5 T-Aera and 3.0 T-Prisma). Moreover, hardware imperfections were analyzed by determining gradient-nonlinearity spatial-distortion (GNSD) and B_0-inhomogeneity spatial-distortion (B_0ISD) for magnetization-prepared rapid acquisition gradient-echo (MP-RAGE) which has well-known distortion characteristics.

Results In 3.0 T, maximum of *gross*-$GNSD_{overall}$ (Euclidean-sum of gross-$GNSD_i$) and *gross*-B_0ISD for MP-RAGE was 2.77 mm and 0.57 mm, respectively. For this scanner, the mean and maximum of *gross*-$HRSD_{overall}$ for IR-PETRA were 0.63 ± 0.38 mm and 1.91 mm, respectively. In 1.5 T, maximum of *gross*-$GNSD_{overall}$ and *gross*-B_0ISD for MP-RAGE was 3.41 mm and 0.78 mm, respectively. The mean and maximum of *gross*-$HRSD_{overall}$ for IR-PETRA were 1.02 ± 0.50 mm and 3.12 mm, respectively.

Discussion The spatial accuracy of MR images, besides being impacted by hardware performance, scanner capabilities, and imaging parameters, is mainly affected by its imaging strategy and data acquisition scheme. In 3.0 T, even without applying vendor correction algorithms, spatial accuracy of IR-PETRA image is sufficient for generating pseudo-CTs. In 1.5 T, distortion-correction is required to provide this accuracy.

Keywords IR-PETRA · Hardware-related spatial distortion · Pseudo-CTs · Brain-specific phantom

Introduction

In recent years, the radiotherapy treatment planning (RTP) workflow which is entirely relied on the magnetic resonance (MR) imaging (MR-only RTP) has been taken into consideration [1–4]. In this workflow, the target and organ at risk are precisely delineated using multi-contrast MR images [5–8], dose calculations are performed by pseudo-computed tomography (pseudo-CT) image generated from these MR images, and patient positioning is conducted by reconstructing the reference digitally reconstructed radiographs (DRRs) from the pseudo-CT [2–4]. MR images are inherently subject to spatial distortion (SD). SD originates from any unwanted deviations in resonance frequency caused by nonlinearity of gradient fields and the imperfect uniformity of the magnetic field [1, 9–16]. Moreover, the accuracy of dosimetric calculations and patient positioning is mainly affected by the discriminatory power of MR pulse sequence in separating bone from air [2–4, 17, 18]. This discriminatory power is mainly improved using the ultrashort echo time (TE) imaging [2, 17, 19–29]. Among different proposed techniques for this task, the pointwise encoding time reduction with radial acquisition (PETRA) sequence has attracted considerable attention [21, 29, 30]. Moreover, apart from

✉ Iraj Jabbari
i_jabbari@ast.ui.ac.ir

1 Faculty of Advanced Sciences and Technologies, University of Isfahan, Isfahan, Iran

2 Department of Biomedical Engineering, Aliabad Katoul Branch, Islamic Azad University, Aliabad-e-Katoul, Iran

3 Quantitative MR Imaging and Spectroscopy Group, Research Center for Molecular and Cellular Imaging, Tehran University of Medical Sciences, Tehran, Iran

4 Department of Medical Physics and Biomedical Engineering, Tehran University of Medical Sciences, Tehran, Iran

Published online: 06 July 2020

retaining this discriminatory power, it would be beneficial to enhance T1 contrast in the PETRA sequence to achieve other required anatomical information. In general, a relatively low flip angle in PETRA leads to a predominantly proton density-weighted contrast. In inversion recovery-PETRA (IR-PETRA), this image contrast is modified by using 180° standard inversion pulse and stronger T1-weighted images are achieved [31–33].

In conventional PETRA, gradients are ramped-up and stabilized prior to applying radiofrequency excitation pulse and then, data are acquired following transmit/receive (T/R) switching delay [29, 30, 34]. This delay leads to missing data points in the central part of *k*-space and thus, only the outer part of k-space is filled up on 3D radial trajectory using radial half-projections [21, 29, 30]. To compensate these missed data points, the central part of *k*-space is acquired in combination with single-point imaging (SPI) on Cartesian sampling pattern. Utilizing additional SPI causes that the requirement on fast T/R switching is mitigated [30]. In IR-PETRA with a similar acquisition manner, the central part of k-space is acquired after very first inversion pulse (TI_1), and the outer part of *k*-space is filled after the second and subsequent inversion pulses (TI_2s) [31–33]. Thus, TI_1 might greatly affect the contrast of resulting image [31]. Moreover, a wait time (TW) as a recovery period, which is considered between the end of each acquisition and the application of the next inversion pulse also affects signal-to-noise and contrast-to-noise ratio on IR-PETRA images [31–33]. Figure 1 illustrates the IR-PETRA pulse sequence diagram. Moreover, according to Fig. 1, TR_{PETRA} is the time between two RF pulses while TR_{IR} is time between two inversion pulses. IR-PETRA, like the PETRA sequence allows quiet scanning because changes in its gradient amplitude are smooth and gradual at the end of each repetition [29, 32, 33] and its required slew-rate is extremely low [32]. Data are acquired under the constant gradient amplitude and spoiling occurs during the incremental gradient changes at the end of each repetition [21, 29, 30, 35]. Eventually, both parts of k-space in this hybrid acquisition are combined during image reconstruction [29].

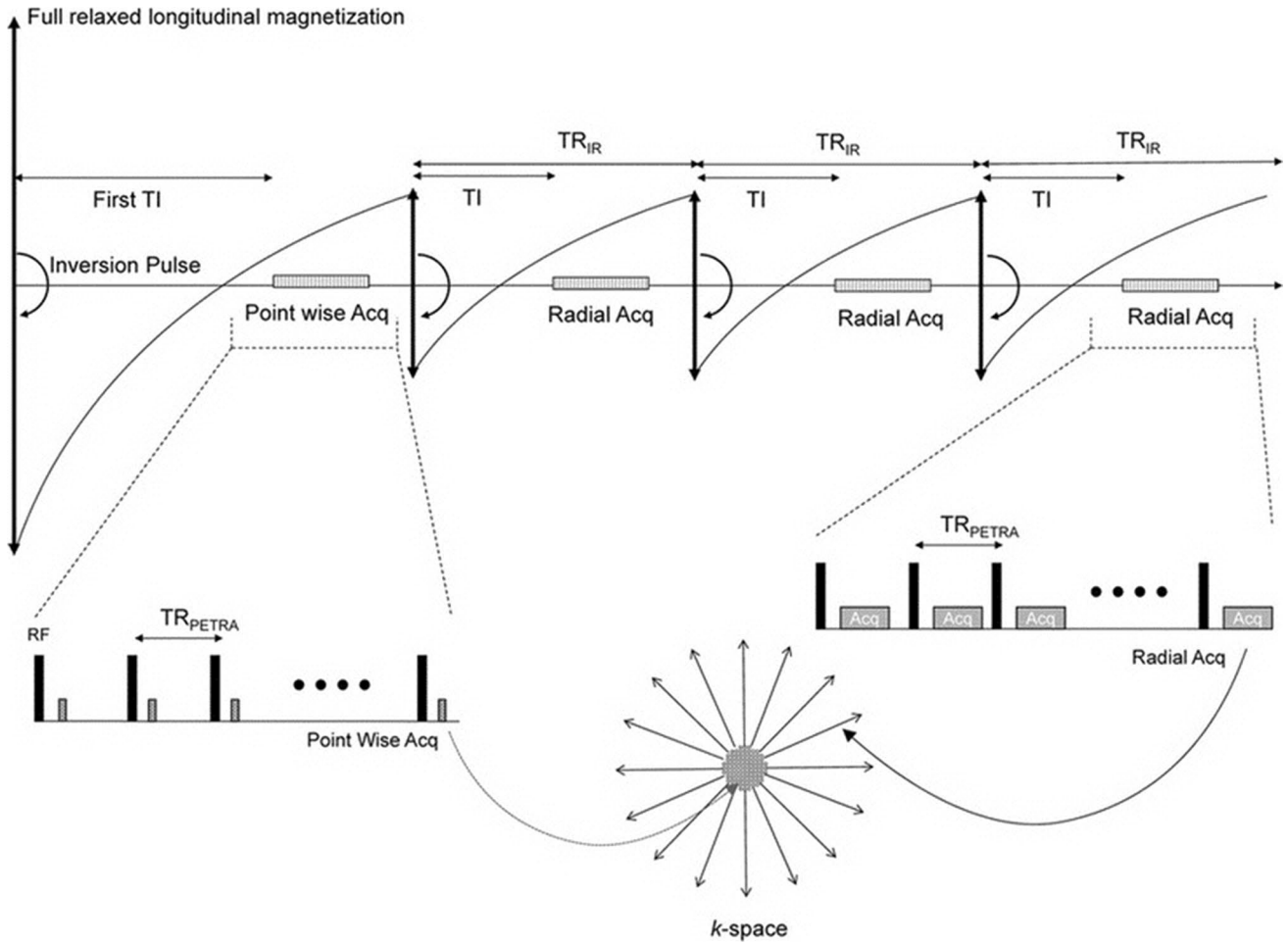

Fig. 1 Pulse sequence diagram for the IR-PETRA sequence

Assessing the SD for IR-PETRA pulse sequence is essential for achieving accurate pseudo-CTs. The SD has been comprehensively evaluated for different spin or gradient echo pulse sequences in several studies [1, 11, 13–15, 29, 36–42]. However, limited study has been performed for PETRA sequence [43] while it requires more precise characterization for MR-only brain RTP purposes.

The SDs can be categorized into two types: patient-related spatial distortion (PRSD) and hardware-related spatial distortion (HRSD) [44]. The PRSD is composed of susceptibility-induced spatial distortion (SISD) and chemical shift-induced spatial distortion (CSISD), and the HRSD, consisting of gradient nonlinearity spatial distortion (GNSD) and B_0-inhomogeneity spatial distortion (B_0ISD). Although SDs induced from off-resonance sources such as SISD, CSISD, and B_0ISD will be minimized by choosing appropriate imaging parameters [41, 45], GNSD as a dominant component of HRSD requires serious assessment [1, 14, 15, 44]. The upper acceptable limit of HRSD for the MR-only RTP workflow is within 2 mm [1, 14, 15, 46, 47]. Other sources which manifest as image degradation and compromise the accuracy of HRSD calculations arise from eddy current (EC) and concomitant gradient fields (CGFs) [48, 49]. EC generated by rapid switching of gradient pulses (gradient slewing) [3, 49] induces additional magnetic field gradients with constant and linear spatial dependence [48, 49] and causes unwanted time-varying gradients and shifts in the main magnetic field [42]. The EC is characterized by different exponential decay time constants included long and short time-constant terms. In general, these EC terms can be compensated by pre-emphasis circuitry and the active shielding of gradient-coil assembly [42]. However, the short time-constant term can be problematic in some types of data acquisition with complex *k*-space trajectory in which data are sampled using high slew-rate, time-varying readout gradient waveforms [1, 3, 42, 50, 51]. In this situation, EC can be compensated in image reconstruction by measuring *k*-space trajectory or a gradient impulse response function [52–54]. For IR-PETRA, the contribution of this term is negligible as compared to other short-T2 imaging techniques such as the conventional ultrashort echo (UTE) which has center-out k-space trajectory and data sampling during gradient ramping with high slew-rate [29, 55]

CGFs originating from Maxwell's equations are a series of undesired magnetic fields which are created simultaneously with the spatial encoding gradient fields and cause unwanted phase accumulation within the measured *k*-space data [48, 56, 57]. These CGF phase errors affect most phase-sensitive imaging techniques including phase-contrast, echo planar imaging, spiral scans, RARE imaging, GRASE imaging, and spectroscopy [48]. CGFs are present whenever gradients are active [58]. In conventional whole-body MR systems, CGFs are characterized by second-order spatial terms and are dependent on gradient amplitudes, distance from isocenter, and main field strength [59, 60]. They can be corrected using gradient pre-emphasis, alteration of gradient waveforms in the pulse sequence, and phase-corrected image reconstruction [56, 58, 60, 61]. IR-PETRA is expected to be less susceptible to CGF phase accumulation because of spoiling during the incremental gradient changes at the end of each repetition, slow slew-rate, and constant gradient amplitude in radial acquisition [29, 30, 32, 48, 58, 59, 61]

In the present study, the assessment of HRSD for IR-PETRA pulse sequence, as an effective sequence in pseudo-CT generation, has been performed at two magnetic field strengths. To achieve this aim, a new brain-specific phantom was designed and constructed. To assess and interpret the HRSD of this hybrid sequence, hardware imperfections, as pre-analysis, are additionally determined using MP-RAGE pulse sequence, which allows separation of GNSD and B_0ISD components duo to its 3D-Cartesian acquisition.

Materials and methods

Theory

HRSD is calculated by comparing control point (CP) locations between CT and MR images of a grid-type phantom [13, 44]. HRSD composed of two components including GNSD and B_0ISD is proportional to the ratio of magnetic field perturbation to gradient amplitude [1, 14]. The calculation of the HRSD and quantitative separation of these two components along each encoding direction determines and explains the hardware imperfections. In the 3D-Cartesian acquisition, GNSDs exist in all encoding directions; while, B_0ISD is observed only in the frequency encoding direction [9, 44]. In 3D-radial acquisitions, this separation is more complicated as they do not have a unique frequency encoding direction [21, 62, 63].

Given that in the Cartesian acquisition like MP-RAGE, data sampling is performed after the decay of short time-constant EC term, it is inherently robust against this term [42]. Moreover, in this acquisition where the transverse magnetization component is usually spoiled and thus the previous CGF phase accumulation will be rewound and not affect the later echo [59, 60], the effect of CGFs is negligible.

Accordingly, in these acquisitions, HRSD is attributed to the GNSDs and B_0ISD components which can be separated by averaging two datasets with an opposite frequency encoding direction (AP and PA) [1, 14, 38, 39]:

$$y_{MR}\big|^{AP} = y_{CT} + \frac{dB_{G_y}(x,y,z)}{G_y} + \frac{dB_0(x,y,z)}{G_y} \quad (1)$$

$$y_{MR}\big|^{PA} = y_{CT} + \frac{dB_{G_y}(x,y,z)}{G_y} - \frac{dB_0(x,y,z)}{G_y}, \quad (2)$$

where $y_{MR}\big|^{AP}$ and $y_{MR}\big|^{PA}$ are the y-locations of CPs in both MR datasets and y_{CT} is the corresponding real y-location in CT image, dB_{G_y}, G_y and dB_0 are the y-gradient field nonlinearity, y-gradient amplitude, and B0-inhomogeneity, respectively. Based on these equations, $GNSD_y$ and B_0ISD components are calculated as follows:

$$GNSD_y = \frac{y_{MR}\big|^{AP} + y_{MR}\big|^{PA}}{2} - y_{CT} \quad (3)$$

$$B_0ISD = y_{MR}\big|^{AP} - y_{CT} - GNSD_y \quad (4)$$

$GNSD_i$ and $HRSD_i$ ($i = x$ and z) are easily calculated because B_0ISD does not affect these directions. In general, the overall magnitudes of $GNSD_i$s ($GNSD_{overall}$) and $HRSD_i$s ($HRSD_{overall}$) are calculated as follows:

$$GNSD_{overall} = \sqrt{(GNSD_x)^2 + (GNSD_y)^2 + (GNSD_z)^2} \quad (5)$$

$$HRSD_{overall} = \sqrt{(GNSD_x)^2 + (GNSD_y + B_0ISD)^2 + (GNSD_z)^2} \quad (6)$$

Considering that in this context, HRSD, GNSD will refer to $HRSD_{overall}$, $GNSD_{overall}$, respectively. Nonlinearities of gradient systems are considerably corrected by applying 3D vendor gradient nonlinearity correction [1, 11, 13, 40]. Moreover, the inhomogeneity of the magnetic field is properly compensated using second-order shim coils [41].

In this context, *gross* distortions will refer to the analysis of acquired images without applying 3D vendor gradient nonlinearity correction and with applying default shimming mode. On the other hand, *residual* distortions will refer to the analysis of acquired images after applying 3D vendor gradient nonlinearity correction and applying standard-shimming mode for achieving better B0-homogeneity. By assessing *gross* distortion, the distortion induced by the actual hardware imperfections such as gradient nonlinearities, limitations of coil design, and B0-inhomogeneity is determined. Also, by evaluating *residual* distortion, the performance of these vendor correction algorithms and residual hardware imperfections can also be identified.

Although various methods have been proposed for the assessment of B_0-homogeneity (H_B (ppm)) [9, 15, 44], in this study, it was calculated using the quantified *residual*-B_0ISD component:

$$H_B = \frac{(residual B_0ISD) \times G_y}{B_0(x,y,z)}, \quad (7)$$

where B_0 (x, y, z) is the main magnetic field in Tesla (T).

Phantom design

A cylindrical brain-specific phantom consisting of 19 clear acrylic plates (Year Long Industrial Co.) with 190 ± 0.1 mm diameter and 10 ± 0.1 mm thickness was designed and constructed (Fig. 2). These plates were located inside an acrylic cylinder with an internal diameter and length of 192 ± 0.1 mm and 200 ± 0.1 mm, respectively. CPs with a diameter of 3 ± 0.1 mm and a radial center-to-center spacing of 11.5 ± 0.1 mm were drilled in all plates in a radial configuration. The CP configurations for two consecutive plates have offset patterns to ensure a precise 3D coverage at different angles and radii. Moreover, this configuration allows for more accurate extraction of the 3D deformable transformation matrix and preserves the details of distortion maps across the phantom volume. Each even and odd plate contains 280 and 248 CPs, respectively, and overall CPs across the phantom volume are 5032. To reduce susceptibility artifact, the phantom was filled with pure paraffin mineral oil with a density of 0.83 g/cm^3. The phantom size and shape were

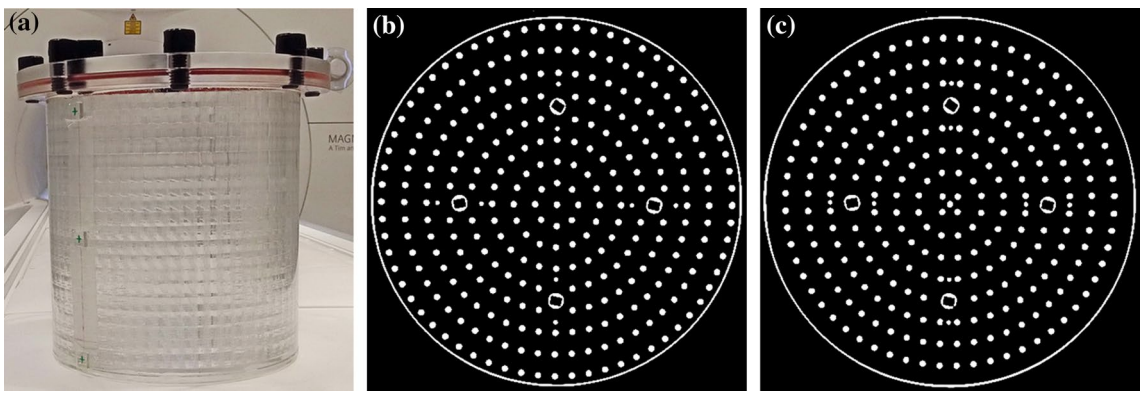

Fig. 2 Constructed phantom (**a**), MR images of the even (**b**) and odd (**c**) plates

designed such that it fitted into the 20-channel head/neck coil. Moreover, a precise slot plus three external markers was considered along the phantom length, which allows to ensure accurate positioning during imaging sessions.

MRI data acquisition

Two clinical pulse sequences including MP-RAGE and IR-PETRA were assessed. All MR imaging were performed on a 1.5 T Magnetom Aera and 3.0 T Magnetom Prisma scanners (Siemens Healthcare, Erlangen, Germany) by using 20-channel head/neck coil. The phantom was oriented along the axial direction. This phantom was precisely positioned at the magnet isocenter when the laser light is aligned with the central external marker in the middle of the phantom length. Moreover, to ensure that phantom was located in the center of FOV in all imaging sessions, the reference point was superimposed on this central external marker in the sagittal localizer image. The key gradient specifications such as maximum gradient amplitude (G_{max}) and slew-rate are 45 mT/m and 200 T/m/s in the 1.5 T scanner and 80 mT/m and 200 T/m/s in the 3.0 T scanner, respectively. In both scanners, gradient nonlinearities were corrected using the 3D method provided by the vendor based on the spherical harmonic polynomial model. In addition, better B0-homogeneity was achieved using standard-shimming mode due to automated inline adjustment based on selected imaging protocols. MP-RAGE pulse sequence was acquired with the following imaging parameters: TE/TR/TI = 3.05/1940/980 ms, flip angle = 9°, BW = 440 Hz/pixel, number of signal averages (NSA) = 3, and T_A = 25 min 54′ at the 1.5 T and TE/TR/TI = 2.40/1900/900 ms, flip angle = 9°, BW = 440 Hz/pixel, NSA = 1, and T_A = 8 min 29′ at 3.0 T. These images were acquired in an axial plane with and without applying 3D vendor gradient nonlinearity correction and using default shimming as well as standard shimming. The in-plane pixel size and slice thickness were 0.5×0.5 mm^2 and 1 mm, respectively. These parameters for IR-PETRA pulse sequence were the following: $TE/TR_{PETRA}/TR_{IR}$ = 0.07/3.37/2250 ms, TI_1/TI_2 = 1300/500 ms, TW = 306 ms, flip angle = 6°, radial spokes = 65,000, BW = 440 Hz/pixel and T_A = 6 min 31′ at the 1.5 T and $TE/TR_{PETRA}/TR_{IR}$ = 0.07/3.61/2250 ms, TI_1/TI_2 = 1300/500 ms, TW = 306 ms, flip angle = 6°, radial pokes = 65,000, BW = 440 Hz/pixel and T_A = 6 min 31′ at 3.0 T. These images were acquired in an axial plane without applying 3D vendor gradient nonlinearity correction and using default shimming mode. The in-plane pixel size and slice thickness were 1.0×1.0 mm^2 and 1 mm, respectively. Note that a few slices were eliminated from all datasets due to partial volume effects.

CT data acquisition

CP locations measured by CT were considered as ground truth due to its superior spatial accuracy [14–16, 44, 64]. The images were acquired by SOMATOM Emotion CT scanner (Siemens Healthcare, Forchheim, Germany) at 110 kV–297 mA. CT image was acquired in the axial plane with FOV of 256 mm, in-plane pixel sizes of 0.5×0.5 mm^2, and the slice thickness of 1 mm.

HRSD assessment

For the assessment of HRSD, an in-house MATLAB-based software consisting of the following sections was developed: (1) image pre-processing (denoising of CT images and intensity inversion of MR images), (2) accurate and automated identification of CPs based on an adaptive threshold method [13], (3) estimation of the CP coordinates based on the circular Hough transform (CHT) algorithm [65], (4) 3D rigid registration using coherent point drift (CPD) algorithm [66], (5) 3D non-rigid registration using CPD algorithm [67], (6) calculation of deformable transformation matrix [16],

and (7) calculation and quantification of the HRSD [1, 11, 14, 40, 44]. The assessment and quantification procedures of HRSD are shown (Fig. 3).

In this assessment, the CPs are detected by applying automatic, fast, and straightforward algorithms. We used a 12-Core CPU (64 GB random access memory) and the computation time of this step for each image being about 10 min. The accuracy of this algorithm in detecting the neighboring CPs was 0.2 pixel. Moreover, the MR images were rigidly registered to the CT image to unify imaging frameworks, while non-rigid registrations were applied for driving the deformable transformation matrix (HRSD map). In addition, the accuracy of the calculated HRSD map and its quantified components were improved using the landmark-based registration algorithm of CPD. By optimizing the registration parameters including β (width of smoothing Gaussian filter) and λ (regularization weight) [66], a high registration accuracy ($\approx$ 0.02 pixel) was achieved. The computation time of this registration for each dataset with the mentioned system was about 120 min. The distortions arising from hardware imperfections of both scanners were quantified for MP-RAGE sequence which has a 3D Cartesian acquisition with well-known and predictable distortion characteristics [13–15, 38, 39]. Quantification for this sequence included *gross* and *residual* magnitudes of $GNSD_i$, $GNSD_{overall}$, B_0ISD, $HRSD_i$, and $HRSD_{overall}$. For IR-PETRA sequence, only *gross*-$HRSD_i$ and *gross*-$HRSD_{overall}$ were quantified. These gross quantifications reveal the maximum distortion due to actual hardware imperfection manifested for this hybrid acquisition. Moreover, because of its non-Cartesian

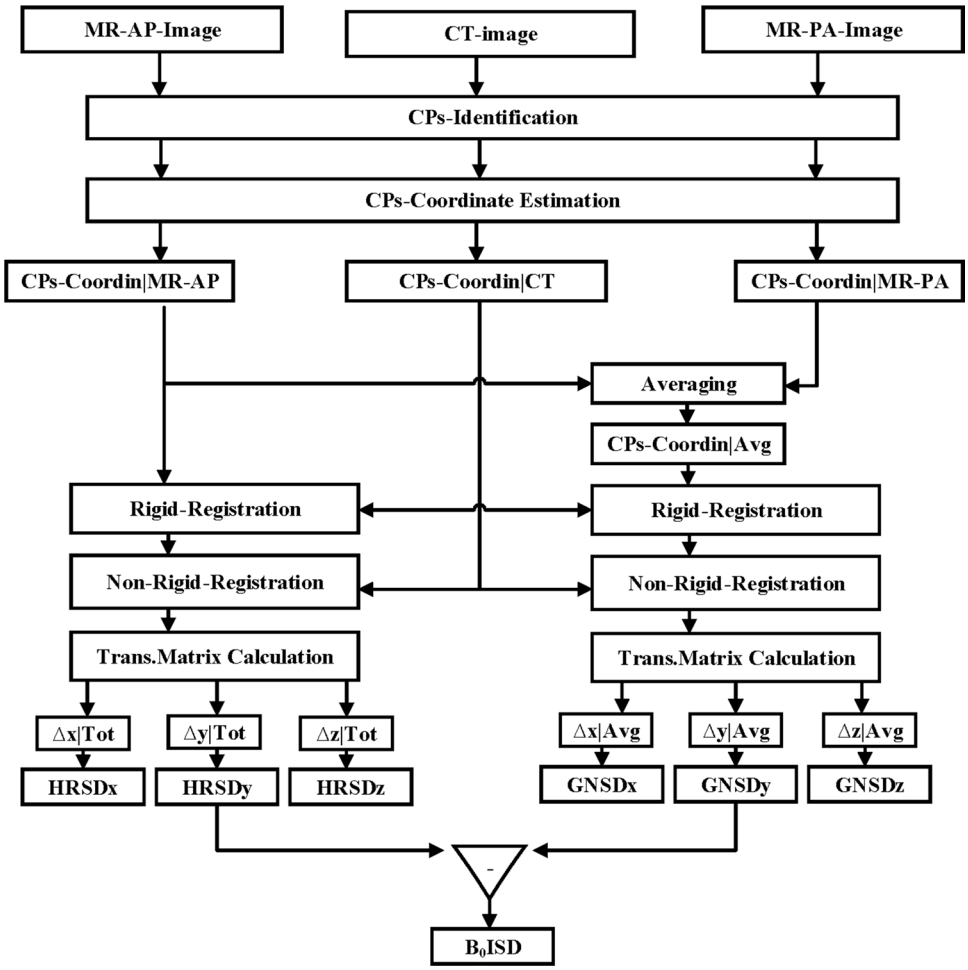

Fig. 3 HRSD, GNSD, and B_0ISD assessment flowchart

acquisition, no separation in $GNSD_i$ and B_0ISD was possible here.

Results

Determination of hardware imperfections based on MP-RAGE sequence

The extremum values of *gross*-$GNSD_{overall}$ and *gross*-B_0ISD components along the through-plane direction ($\pm z$) for MP-RAGE sequence of both scanners are shown in Fig. 4. In Fig. 4a and b, the extremum values shown as an "error bars" indicate the highest and lowest values of *gross*-$GNSD_{overall}$, while the highlighted points correspond to its mean values for each slice. Similar plots for the *gross*-B_0ISD component are presented in Fig. 4c and d. As can be seen, the highest mean values of *gross*-$GNSD_{overall}$ occur towards higher $|z|$. The extremum values of *gross*-B_0ISDs are randomly distributed and their mean values fluctuate around zero.

In Fig. 5, the in-plane *gross*-$GNSD_i$ ($i = x$ and y) maps are demonstrated at $z = -90$ mm. As shown, the magnitude of *gross*-$GNSD_i$ along phase and frequency encoding directions in the 3.0 T scanner are less than that of the 1.5 T scanner.

The statistical results for the *gross*- and *residual*-$GNSD_i$ ($i = x$, y, and z) and *gross*- and *residual*-$GNSD_{overall}$ are summarized in Table 1. Similar results are reported for *gross*- and *residual*-B_0ISD as well as H_B in Tables 2 and 3, respectively.

Calculation of *gross*-HRSD for IR-PETRA pulse sequence

As mentioned, *gross*-HRSD for IR-PETRA is presented and compared to explain the impact of the actual hardware imperfections and data acquisition scheme in spatial distortion. Figure 6 shows the maximum and mean values of *gross*-$HRSD_{overall}$ along the through-plane direction for IR-PETRA and MP-RAGE pulse sequences in both scanners.

The patterns of in-plane *gross*-$HRSD_{overall}$ map for IR-PETRA and MP-RAGE sequences are demonstrated in Figs. 7 and 8, respectively, at $z = \pm 90$ mm in which the highest *gross*-$HRSD_{overall}$ is anticipated for both scanners. In these figures, the in-plane patterns of *gross*-$HRSD_{overall}$ map

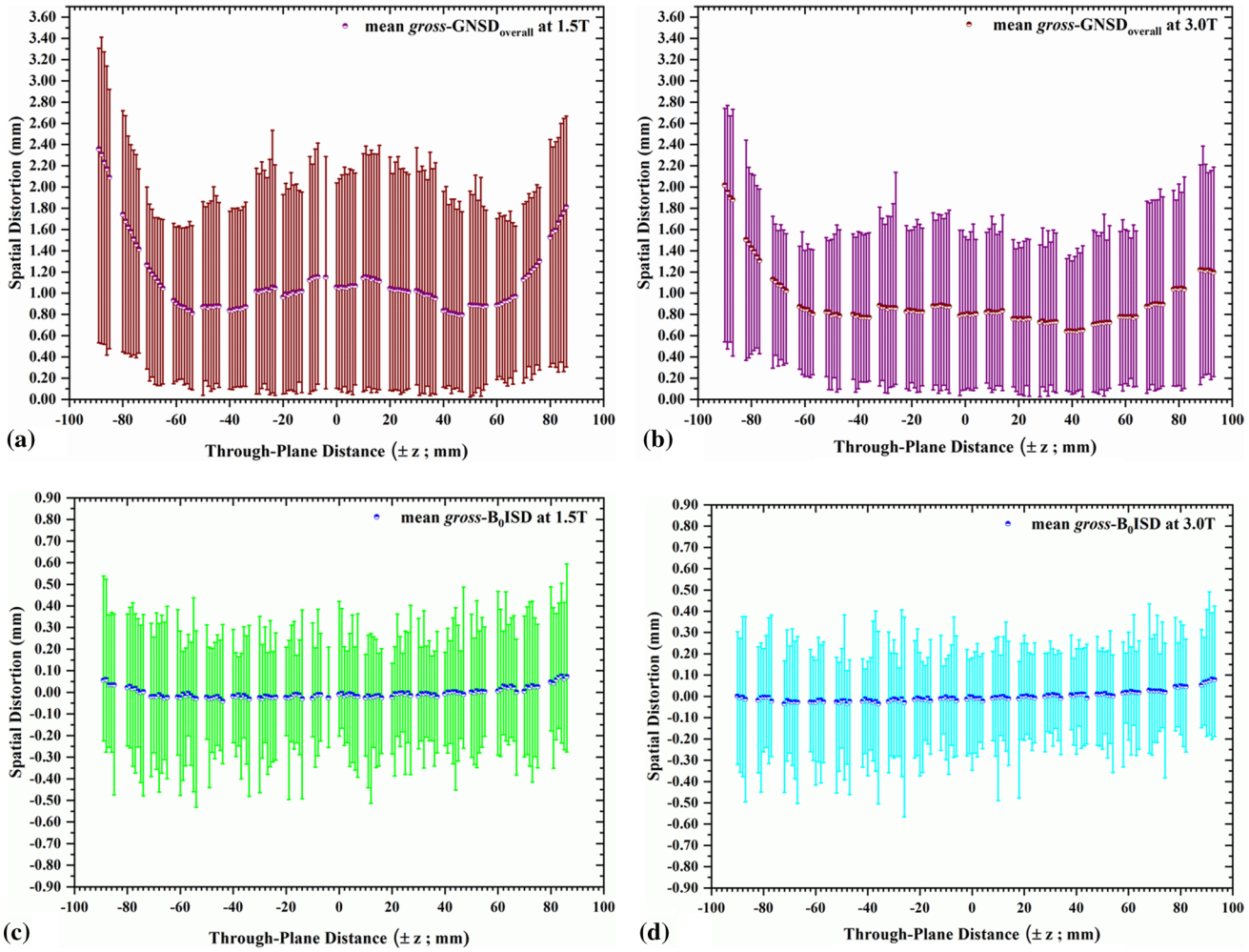

Fig. 4 Extremum (line) and mean values (dots) of through-plane *gross*-$GNSD_{overall}$ and *gross*-B_0ISD for MP-RAGE sequence: **a** *gross*-$GNSD_{overall}$ at 1.5 T, **b** *gross*-$GNSD_{overall}$ at 3.0 T, **c** *gross*-B_0ISD at 1.5 T, and **d** *gross*-B_0ISD at 3.0 T

are irregular for both sequences (even within a given radius) and are asymmetrically distributed along the through-plane direction. For example, for IR-PETRA sequence at $z=-90$ mm and $z=+90$ mm, the CPs subjected to *gross*-$HRSD_{overall}$ of more than 2 mm are 30.38% and 18.80% in the 1.5 T, respectively, and zero in the 3.0 T. At $z=0$, these values reduce to 3.2% and zero in the 1.5 T and 3.0 T, respectively. For the MP-RAGE sequence, at $z=-90$ mm and $z=+90$ mm, the corresponding values are 57.90% and 20.30% in the 1.5 T and 23.40% and 10.15% in the 3.0 T, respectively. At $z=0$, these values are almost zero in both scanners.

The statistical results of the *gross*-$HRSD_i$ ($i=x$, y, and z) and gross-$HRSD_{overall}$ for IR-PETRA and MP-RAGE sequences are presented in Table 4 in both scanners. In Fig. 9, the histograms of the *gross*-$HRSD_i$ ($i=x$, y, and z) and *gross*-$HRSD_{overall}$ are shown for IR-PETRA sequence of both scanners.

Discussion

The performance of MR-only RTP workflow which depends on the accuracy of pseudo-CT generation is mainly affected by HRSD in MR images as well as the bone–air discrimination power of MR pulse sequence [2–4, 17, 18]. Accordingly, assessing the HRSD for IR-PETRA sequence, which improved this discrimination, is essential for achieving the effective performance [21, 42]. Although HRSD for conventional pulse sequences has been evaluated in previous studies [1, 11, 13, 14, 37, 40, 44, 46, 64, 68, 69], its characterization for IR-PETRA has remained understudied [43]. In the study by Law et al. [43], the mean value of residual HRSD (after applying gradient nonlinearity correction) was calculated using a large phantom with isotropic CPs pattern across the phantom volume ($55\times55\times32.5cm^3$, 3892 spherical CPs with 6 mm-diameter and 25 mm-isotropic interval). All images were acquired using integrated body coil in the

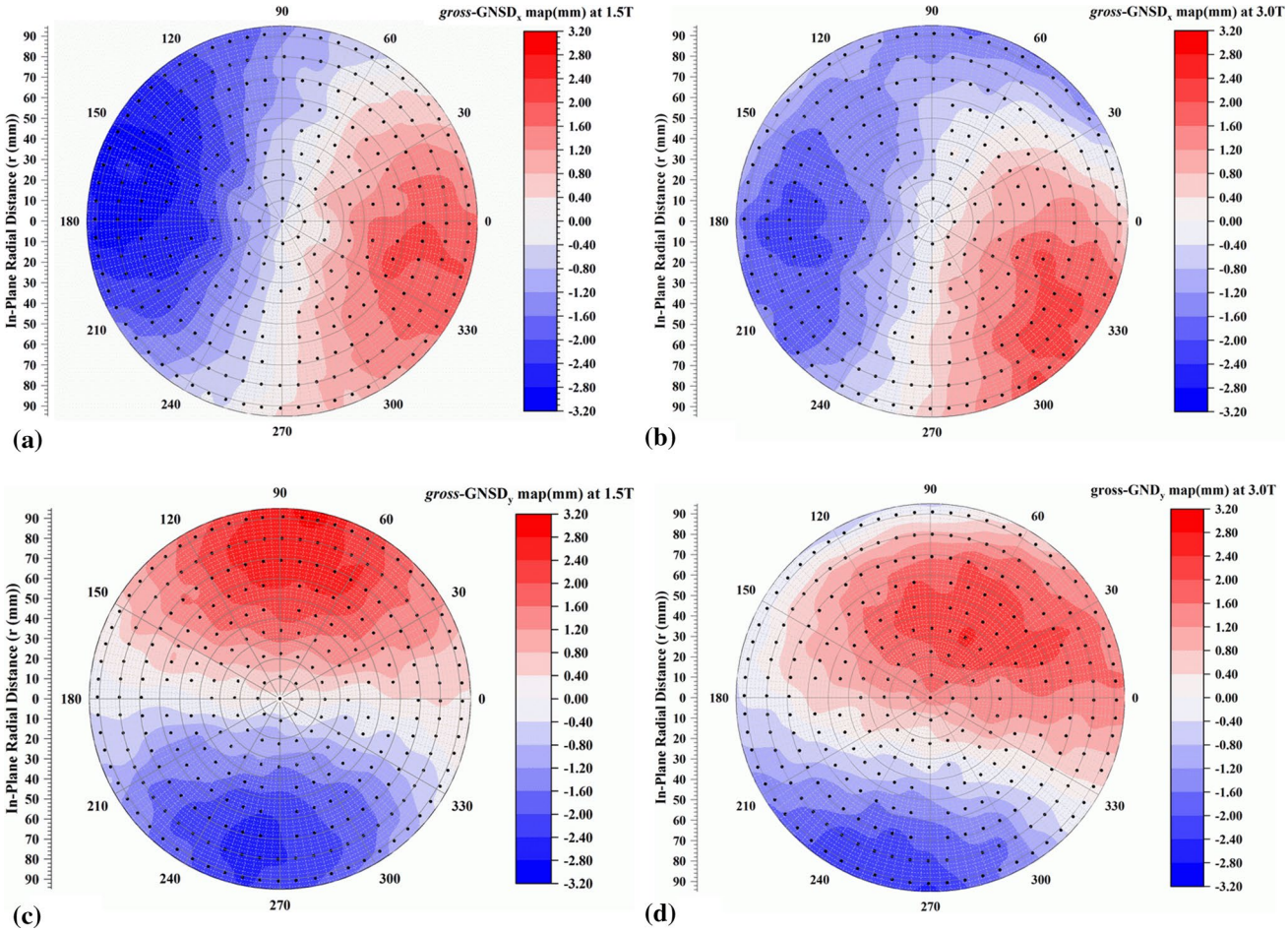

Fig. 5 In-plane *gross*-GNSD$_i$ maps for MP-RAGE sequence at $z = -90$ mm. **a** *gross*-GNSD$_x$ at 1.5 T, **b** *gross*-GNSD$_x$ at 3.0 T, **c** *gross*-GNSD$_y$ at 1.5 T, and **d** *gross*-GNSD$_y$ at 3.0 T

Table 1 Statistical results of the *gross*- and *residual*-GNSD$_i$ ($i = x$, y, and z) and *gross*- and *residual*-GNSD$_{overall}$ for MP-RAGE sequence at 1.5 T and 3.0 T scanners

Component	Strength (T)	Type	Range (mm)	Mean ± SD (mm)	%CP > |0.5| mm	%CP > |1| mm	%CP > |1.5| mm	%CP > |2| mm
GNSD$_x$	1.5	*gross*	(− 3.20 to 2.48)	0.05 ± 0.72	42.73	16.73	3.50	1.36
		residual	(− 1.65 to 1.64)	0.00 ± 0.33	11.76	1.34	0.02	0.00
	3.0	*gross*	(− 2.27 to 2.38)	0.03 ± 0.54	31.94	6.06	1.38	0.21
		residual	(− 1.57 to 1.59)	0.00 ± 0.40	20.96	1.63	0.02	0.00
GNSD$_y$	1.5	*gross*	(− 2.62 to 2.92)	0.03 ± 0.66	40.08	12.73	3.08	0.86
		residual	(− 1.25 to 1.13)	0.00 ± 0.32	12.90	0.11	0.00	0.00
	3.0	*gross*	(− 2.53 to 2.53)	0.01 ± 0.53	27.60	6.42	1.78	0.45
		residual	(− 1.52 to 1.62)	0.00 ± 0.37	16.51	1.75	0.00	0.00
GNSD$_z$	1.5	*gross*	(− 1.75 to 1.68)	0.01 ± 0.76	57.72	21.89	2.00	0.00
		residual	(− 1.68 to 1.66)	0.00 ± 0.81	61.30	27.36	2.60	0.00
	3.0	*gross*	(− 1.49 to 1.34)	0.00 ± 0.67	53.02	14.71	0.00	0.00
		residual	(− 1.26 to 1.29)	0.00 ± 0.64	51.57	12.31	0.00	0.00
GNSD$_{overall}$	1.5	*gross*	(0.02 to 3.41)	1.11 ± 0.55	85.84	54.34	23.51	7.26
		residual	(0.01 to 2.19)	0.83 ± 0.43	73.47	35.71	7.58	0.03
	3.0	*gross*	(0.03 to 2.77)	0.91 ± 0.44	81.58	38.64	9.00	1.92
		residual	(0.03 to 2.00)	0.77 ± 0.35	72.59	26.90	2.28	0.00

Table 2 Statistical results of the *gross*- and *residual*-B_0ISD (mm) for MP-RAGE sequence at 1.5 T and 3.0 T scanners

Component	Strength (T)	Type	Range (mm)	Mean ± SD (mm)	%CP > |0.1| mm	%CP > |0.2| mm
B_0ISD	1.5	*gross*	(− 0.78 to 0.60)	0.00 ± 0.09	22.52	1.67
		residual	(− 0.33 to 0.31)	0.00 ± 0.05	7.14	0.00
	3.0	*gross*	(− 0.57 to 0.49)	0.00 ± 0.08	16.18	0.84
		residual	(− 0.26 to 0.29)	0.00 ± 0.03	4.51	0.00

Table 3 Statistical results of the H_B (ppm) calculated from *residual*-B_0ISD component for MP-RAGE sequence at 1.5 T and 3.0 T scanners

Component	Strength (T)	Range (ppm)	Mean ± SD (ppm)	%CP > |1| ppm
H_B	1.5	(− 4.55 to 4.26)	0.00 ± 0.58	2.58
	3.0	(− 1.78 to 2.00)	0.00 ± 0.21	0.45

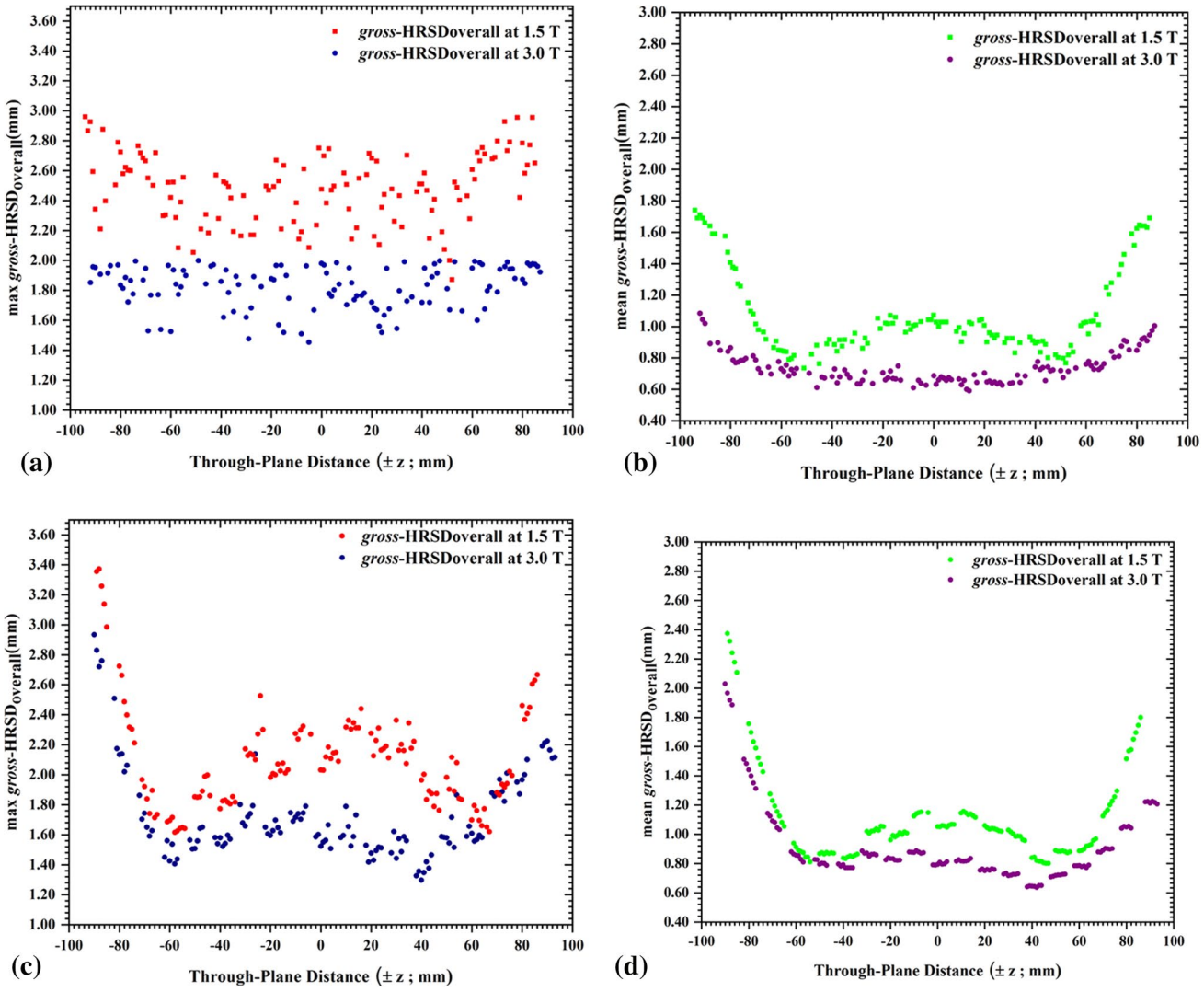

Fig. 6 Through-plane *gross*-$HRSD_{overall}$ at 1.5 T and 3.0 T scanners. For IR-PETRA sequence, the maximum (**a**) and mean value (**b**), and for MP-RAGE sequence, maximum (**c**) and mean value (**d**)

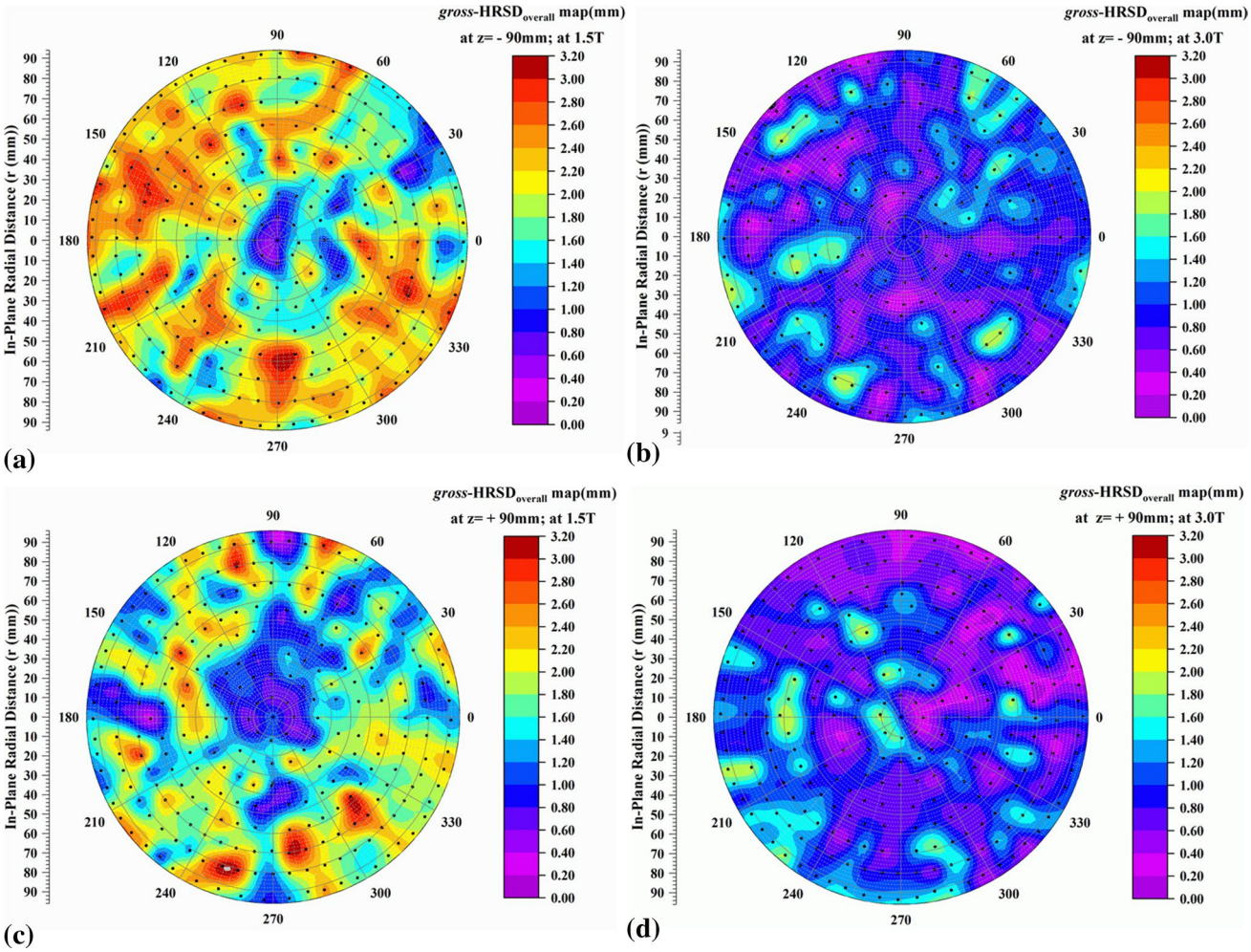

Fig. 7 In-plane *gross*-$HRSD_{overall}$ for IR-PETRA sequence at **a** $z = -90$ mm at 1.5 T, **b** $z = -90$ mm at 3.0 T, **c** $z = +90$ mm at 1.5 T, and **d** $z = +90$ mm at 3.0 T

1.5 T scanner. The mean value of *residual*-HRSD for IR-PETRA was reported 0.4 ± 0.17 mm for FOV of 200 mm [43]. The highest magnitude of *residual*-HRSD was found in the axial orientation, confirming the importance of this orientation for precise HRSD evaluation of IR-PETRA. In that study, the *gross*-HRSD were not calculated, which can be attributed to failure of CPs' detection due to the severity of distortion magnitude at larger distances from scanner's isocenter as well as the isotropic distribution of the CPs across the phantom volume.

In this study, we aimed to precisely characterize *gross*-HRSD for IR-PETRA in head region. This characterization, apart from evaluating the required spatial accuracy for MR-only brain RTP purposes, interprets the impacts of the actual hardware imperfections, restrictions of sequence and scanner, imaging strategy, and data acquisition scheme in degrading of this accuracy. To overcome the limitations resulting from the lower SNR and sensitivity variation of RF-coil across the imaging volume which can compromise the accuracy of HRSD maps, all images were acquired with a 20-channel head/neck coil and after applying pre-scan normalization. To this aim, a brain-specific phantom was designed and constructed. As per analysis, hardware imperfections were quantified by MP-RAGE. This acquisition is robust to short time constant EC term and CGF-induced phase errors; thus, imperfections are generally attributed to the GNSD and B_0ISD components.

The evaluation of hardware imperfections for the MP-RAGE sequence indicates that the both gross and residual magnitudes of GNSD and B_0ISD in the 3.0 T scanner are lower than those in the 1.5 T scanner. Based on Table 1, the highiest *gross*-$GNSD_i$ (> 2 mm) is observed along the *x*- and *y*-axes indicating higher gradient nonlinearity along these axes, in both scanners. Applying the vendor gradient nonlinearity correction leads to a symmetrical distribution of a *residual*-$GNSD_i$ along all axes and mitigates it to an acceptable limit (< 2 mm) in both scanners. Most CPs are subject to *residual*-$GNSD_{overall}$ of less than 1.5 mm, especially in the

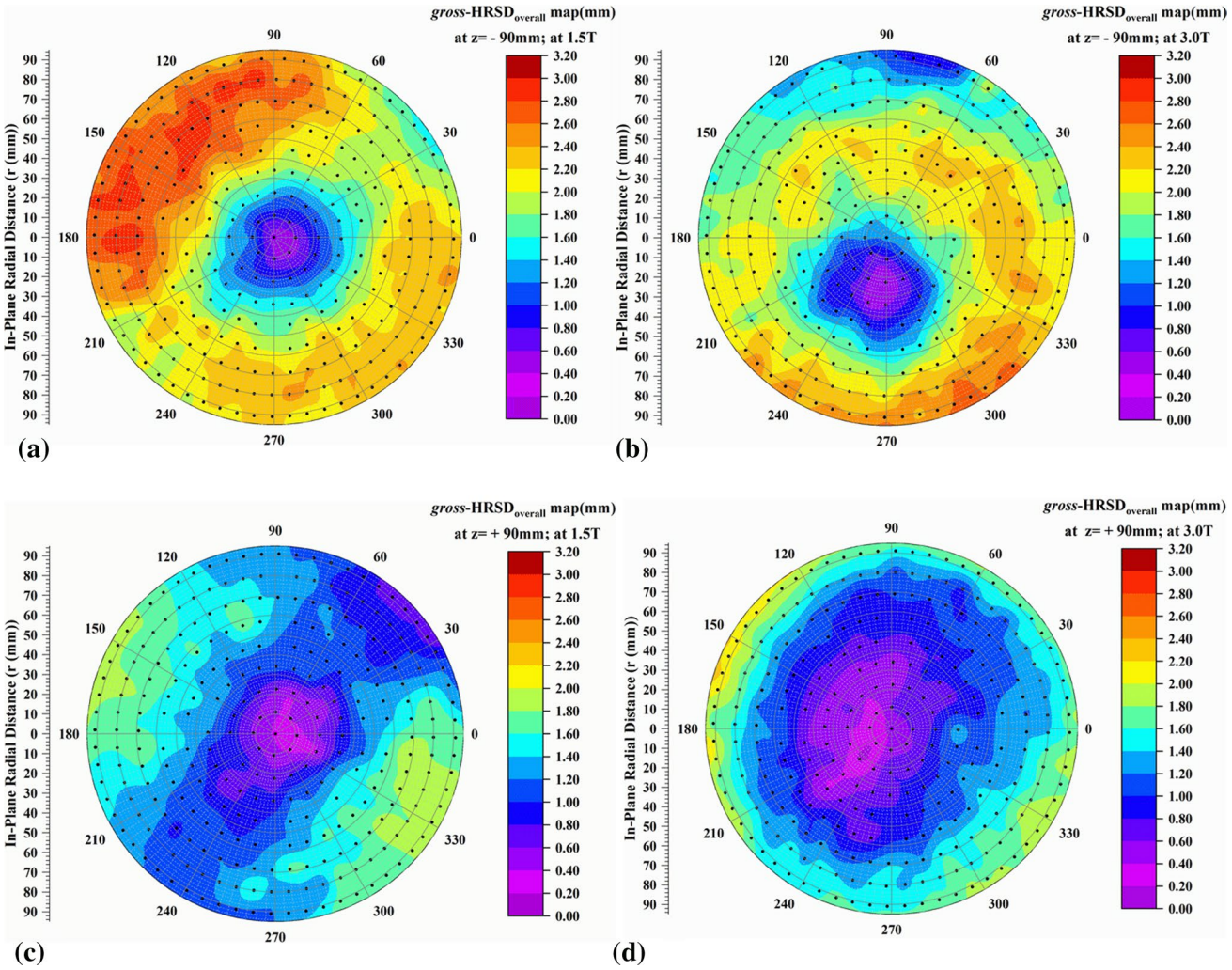

Fig. 8 In-plane *gross*-$HRSD_{overall}$ for MP-RAGE sequence at **a** $z=-90$ mm at 1.5 T, **b** $z=-90$ mm at 3.0 T, **c** $z=+90$ mm at 1.5 T, and **d** $z=+90$ mm at 3.0 T

3.0 T scanner. Despite the appropriate performance of the vendor gradient nonlinearity correction which was observed in the 1.5 T scanner, *residual*-$GNSD_i$ and *residual*-$GNSD_{overall}$ in the 3.0 T scanner were still lower than those of the 1.5 T scanner. According to the results of Table 2, most CPs are subject to a *gross*-B_0ISD of less than 0.2 mm and after applying standard-shimming mode due to improvement of H_B, *residual*-B_0ISD in most CPs decreases to less than 0.1 mm, in both scanners. As a result, due to high magnitude of *gross*-$GNSD_x$ and *gross*-$GNSD_y$ as dominant components of HRSD, a high magnitude of *gross*-$HRSD_x$ and *gross*-$HRSD_y$ (>2 mm) is justifiable for MP-RAGE (Table 4). Although a high magnitude of *gross*-$HRSD_y$ can be attributed to the simultaneous occurrence of *gross*-$GNSD_y$ and *gross*-B_0ISD in the frequency encoding direction, this high value for *gross*-$HRSD_x$ reveals a higher gradient nonlinearity along the phase encoding direction. For IR-PETRA, the evaluation of quantified *gross*-$HRSD_i$ shows that the higher perturbation also occurs along the *x*- and *y*-axes in both scanners, as expected. As a conclusion, due to the better hardware performance of the 3.0 T scanner such as higher gradient linearity, improved coil design, and better magnetic shimming, a lower HRSD magnitude is predicted for IR-PETRA in the 3.0 T. The obtained results (Table 4) confirm that the maximum *gross*-$HRSD_{overall}$ for IR-PETRA is within the acceptable limit in the 3.0 T. Moreover, most of the CPs are subject to a *gross*-$HRSD_{overall}$ of less than 1.5 mm, in the 3.0 T. In the 1.5 T scanner, a small number of the CPs have a *gross*-$HRSD_{overall}$ of more than 2.0 mm, which occurs even in more critical regions of the FOV with irregular distribution (Fig. 7).

Considering that, the *gross*-$HRSD_{overall}$ for IR-PETRA was low, while the radial projection imaging as applied in UTE sequences is sensitive to scanner imperfection such as

Table 4 Statistical results of the *gross*-HRSD$_i$ ($i = x, y, z$) and *gross*-HRSD$_{overall}$ for IR-PETRA sequence and MP-RAGE sequence at 1.5 T and 3.0 T scanners

Component	Strength (T)	Type	Range (mm)	Mean ± SD (mm)	%CP > |0.5| mm	%CP > |1| mm	%CP > |1.5| mm	%CP > |2| mm
gross-HRSD$_x$	1.5	IR-PETRA	(− 3.11 to 3.07)	0.00 ± 0.68	36.84	14.86	3.17	1.10
		MP-RAGE	(− 3.20 to 2.48)	0.05 ± 0.72	42.73	16.73	3.50	1.36
	3.0	IR-PETRA	(− 1.97 to 1.99)	0.00 ± 0.52	31.08	5.19	1.29	0.00
		MP-RAGE	(− 2.27 to 2.38)	0.03 ± 0.54	31.94	6.06	1.38	0.21
gross-HRSD$_y$	1.5	IR-PETRA	(− 3.10 to 3.11)	0.00 ± 0.68	34.96	11.81	3.03	0.91
		MP-RAGE	(− 2.68 to 3.12)	0.03 ± 0.70	40.21	12.75	3.12	0.93
	3.0	IR-PETRA	(− 1.93 to 1.99)	0.00 ± 0.51	26.53	5.65	1.60	0.00
		MP-RAGE	(− 2.83 to 2.57)	0.01 ± 0.53	27.71	6.64	1.87	0.49
gross-HRSD$_z$	1.5	IR-PETRA	(− 1.14 to 1.15)	0.00 ± 0.45	30.16	0.87	0.00	0.00
		MP-RAGE	(− 1.75 to 1.68)	0.01 ± 0.76	57.72	21.89	2.00	0.00
	3.0	IR-PETRA	(− 0.80 to 0.81)	0.00 ± 0.31	12.60	0.00	0.00	0.00
		MP-RAGE	(− 1.49 to 1.34)	0.00 ± 0.67	53.02	14.71	0.00	0.00
gross-HRSD$_{overall}$	1.5	IR-PETRA	(0.03 to 3.12)	1.02 ± 0.50	82.22	51.70	21.08	6.66
		MP-RAGE	(0.00 to 3.47)	1.11 ± 0.55	85.98	54.34	23.58	7.38
	3.0	IR-PETRA	(0.01 to 1.91)	0.63 ± 0.38	77.81	27.89	6.48	0.00
		MP-RAGE	(0.02 to 2.93)	0.91 ± 0.44	81.69	38.64	9.15	2.01

time delays within the gradient system as well as the short time constant EC term [29, 31, 42, 70]. This result can be explained based on its imaging strategy and data acquisition method. Silent IR-PETRA sequence has a hybrid k-space acquisition scheme composed of a radial part for acquiring high spatial frequency data and a Cartesian part for acquiring low spatial frequency data [21]. Due to the ramp-up and stabilization of gradients before applying the excitation pulse, the data are acquired during the plateau period of the readout gradient at both parts. In IR-PETRA, data are acquired with a constant gradient amplitude at both parts. Moreover, smoothly varying gradients at the end of each repetition allow a silent scanning and the required slew rate is extremely low [31–33]. Considering that, data sampling in the Cartesian part occurs with a lower amplitude, compared to radial part, and with stepwise reducing scheme [29]. Accordingly, the contribution of short time constant EC term and the artifacts originating from time delays in the gradient start are negligible for this sequence [29, 71, 72]. At the end of each repetition, spoiling occurs during the incremental gradient changes and the gradients are ramped up to the needed amplitude [29, 30]. Accordingly, due to spoiling at the end of each repetition, low- and constant gradient amplitude in its radial acquisition as well as its required slow slew-rate [29, 30, 48, 58, 59, 61], IR-PETRA sequence is expected to be less susceptible to CGF phase accumulation in brain scan (18–24 cm). Based on the above considerations it can be expected that IR-PETRA is less influenced by hardware imperfections and application of this preferred sequence is recommended for this workflow to improve the discriminatory power of air from bone. The results of the present study reveal that the spatial accuracy of MR images is strongly affected by hardware imperfections, performance of correction algorithms, imaging strategy, and the data acquisition scheme. The spatial accuracy of the IR-PETRA images acquired by the 3.0 T scanner is sufficient for generating pseudo-CTs, while, this accuracy is achieved by applying distortion correction in 1.5 T scanner. Variations in spatial accuracy of IR-PETRA images emphasize the importance of distortion assessment in each specific scanner using standardized phantom.

Conclusion

The HRSD assessment for IR-PETRA sequence, as an effective sequence for generating pseudo-CTs in MR-only brain RTP workflow, was performed for two magnetic field strengths. The results showed that the *gross*-HRSD$_{overall}$ magnitude for IR-PETRA in the 3.0 T is acceptable for this workflow (even without any gradient nonlinearity correction). This can be attributed to the better hardware performance of this scanner such as optimal gradient linearity and better magnetic shimming. Moreover, in IR-PETRA, as a quiet sequence, the changings in gradient strengths are smooth and gradual at the end of each repetition and the required slew-rate is extremely low. Furthermore, data acquisition is performed with a constant gradient amplitude and spoiling occurs during the incremental gradient changes at the end of each repetition. Accordingly, IR-PETRA was

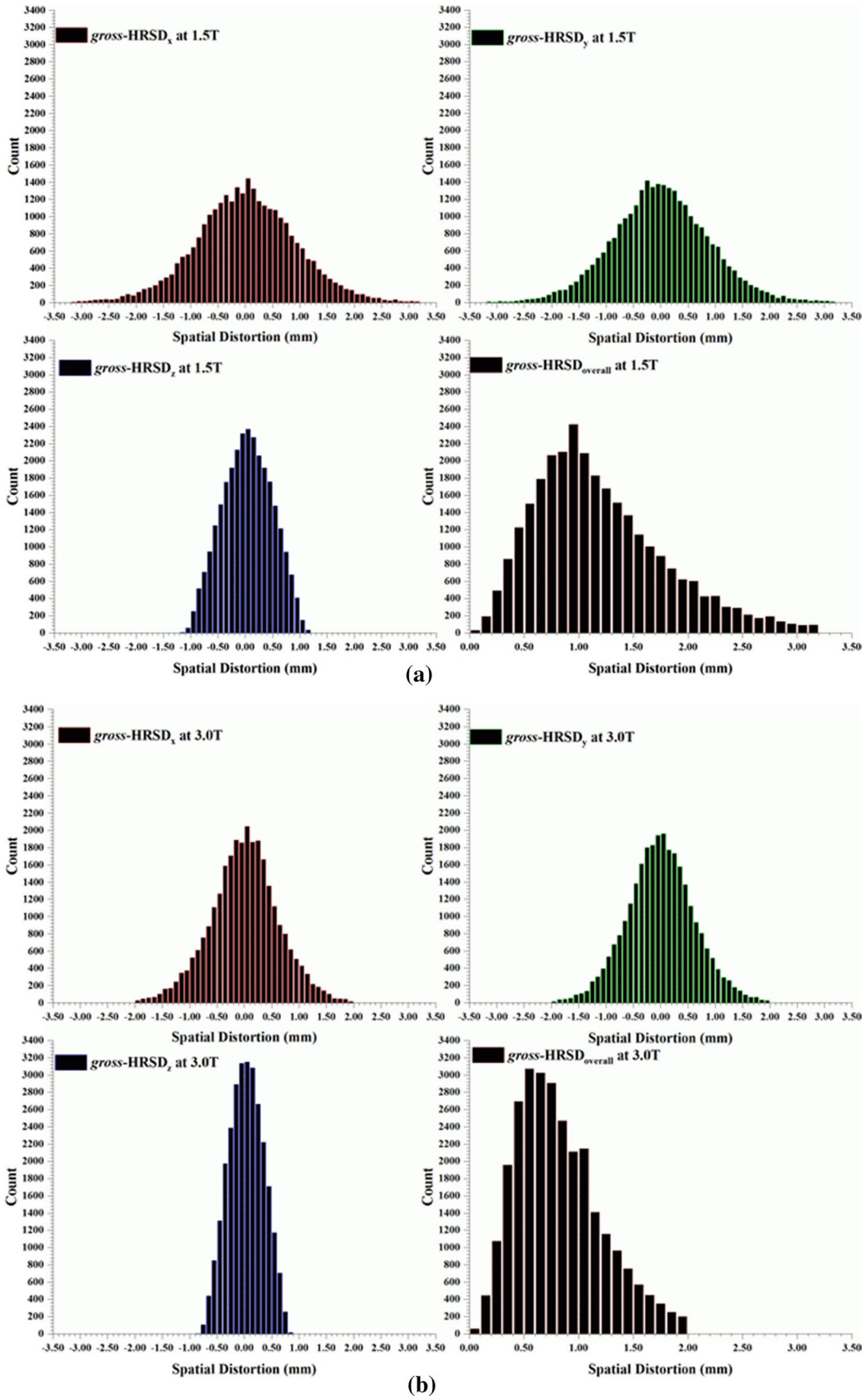

Fig. 9 Histograms of the *gross*-HRSD$_i$ ($i = x$, y, and z) and *gross*-HRSD$_{overall}$ for IR-PETRA sequence at **a** 1.5 T and **b** 3.0 T scanners

less affected by short time constant EC term, time delays within the gradient system and CGF effects in FOV of brain. The assessment results of the 1.5 T show that distortion correction should be applied to the acquired images of IR-PETRA to reduce its *gross*-$HRSD_{overall}$ to less than 2.0 mm.

Acknowledgements This work was technically supported by National Brain Mapping Laboratory (NBML) and Omid Hospital (Tehran, Iran). The authors would like to appreciate Dr. Zahra Alizadeh Sani (Head of CMR department at Omid Hospital), Mr. Mohsen Shojaei Moghaddam (Siemens Clinical Applications Specialist) and Ms. Shaghayegh Karimi Alavijeh (MR-Technologist at NBML).

Compliance with ethical standards

Conflict of interest The authors declare that they have no conflict of interest.

Ethical approval This article does not contain any studies with human participants or animals performed by any of the authors.

References:

1. Baldwin LN, Wachowicz K, Thomas SD, Rivest R, Fallone BG (2007) Characterization, prediction, and correction of geometric distortion in MR images. Med Phys 34(2):388–399
2. Edmund JM, Nyholm T (2017) A review of substitute CT generation for MRI-only radiation therapy. Radiat Oncol 12(1):28
3. Owrangi AM, Greer PB, Glide-Hurst CK (2018) MRI-only treatment planning: benefits and challenges. Phys Med Biol 63(5):1
4. Nyholm T, Jonsson J (2014) Counterpoint: opportunities and challenges of a magnetic resonance imaging–only radiotherapy work flow. Semin Radiat Oncol 24(3):175–180
5. Beigi M, Ghasemi K, Mirzaghavami P, Khanmohammadi M, SalighehRad H (2018) Malignancy probability map as a novel imaging biomarker to predict malignancy distribution: employing MRS in GBM patients. J Neurooncol 138(3):619–625
6. Beigi M, Safari M, Ameri A, Moghadam MS, Arbabi A, Tabatabaeefar M, SalighehRad H (2018) Findings of DTI-p maps in comparison with T 2/T 2-FLAIR to assess postoperative hypersignal abnormal regions in patients with glioblastoma. Cancer Imaging 18(1):33
7. Fathi Kazerooni A, Nabil M, Zeinali Zadeh M, Firouznia K, Azmoudeh-Ardalan F, Frangi AF, Davatzikos C, Saligheh Rad H (2018) Characterization of active and infiltrative tumorous subregions from normal tissue in brain gliomas using multiparametric MRI. J Magn Reson Imaging 48(4):938–950
8. Fathi Kazerooni AMM, Rezaei S, Bakhshandehpour G, Saligheh RH (2015) Multi-parametric (ADC/PWI/T2-w) image fusion approach for accurate semi-automatic segmentation of tumorous regions in glioblastoma multiforme. MAGMA 28:13–22
9. Chen HH, Boykin RD, Clarke GD, Gao JHT, Roby JW III (2006) Routine testing of magnetic field homogeneity on clinical MRI systems. Med Phys 33(11):4299–4306
10. Mattila S, Renvall V, Hiltunen J, Kirven D, Sepponen R, Hari R, Tarkiainen A (2007) Phantom-based evaluation of geometric distortions in functional magnetic resonance and diffusion tensor imaging. Magnet Reson Med 57(4):754–763
11. Karger CP, Höss A, Bendl R, Canda V, Schad L (2006) Accuracy of device-specific 2D and 3D image distortion correction algorithms for magnetic resonance imaging of the head provided by a manufacturer. Phys Med Biol 51(12):N253
12. Runge VM, Kirsch JE, Thomas GS, Mugler JP III (1991) Clinical comparison of three-dimensional MP-RAGE and FLASH techniques for MR imaging of the head. J Magn Reson Imaging 1(4):493–500
13. Stanescu T, Jans HS, Wachowicz K, Fallone BG (2010) Investigation of a 3D system distortion correction method for MR images. J Appl Clin Med Phys 11(1):200–216
14. Walker A, Liney G, Holloway L, Dowling J, Rivest-Henault D, Metcalfe P (2015) Continuous table acquisition MRI for radiotherapy treatment planning: distortion assessment with a new extended 3D volumetric phantom. Med Phys 42(4):1982–1991
15. Walker A, Liney G, Metcalfe P, Holloway L (2014) MRI distortion: considerations for MRI based radiotherapy treatment planning. Austr Phys Eng Sci Med 37(1):103–113
16. Nousiainen K, Mäkelä T (2019) Measuring geometric accuracy in magnetic resonance imaging with 3D-printed phantom and nonrigid image registration. MAGMA 23:1–10
17. Paradis E, Cao Y, Lawrence TS, Tsien C, Feng M, Vineberg K, Balter JM (2015) Assessing the dosimetric accuracy of magnetic resonance-generated synthetic CT images for focal brain VMAT radiation therapy. Int J Radiat Oncol Biol Phys 93(5):1154–1161
18. Hsu S-H, Cao Y, Huang K, Feng M, Balter JM (2013) Investigation of a method for generating synthetic CT models from MRI scans of the head and neck for radiation therapy. Phys Med Biol 58(23):8419
19. Johansson A, Karlsson M, Nyholm T (2011) CT substitute derived from MRI sequences with ultrashort echo time. Med Phys 38(5):2708–2714
20. Johansson A, Karlsson M, Yu J, Asklund T, Nyholm T (2012) Voxel-wise uncertainty in CT substitute derived from MRI. Med Phys 39(6 Part 1):3283–3290
21. Li C (2014) Magnetic resonance imaging of short-T2 tissues with applications for quantifying cortical bone water and myelin. publicly accessible penn dissertations, p 1350. https://www.repositoryupennedu/edissertations/1350.
22. Abbasi-Rad S, Saligheh Rad H (2017) Quantification of human cortical bone bound and free water in vivo with ultrashort echo time MR imaging: a model-based approach. Radiology 283(3):862–872
23. Rad HS, Lam SCB, Magland JF, Ong H, Li C, Song HK, Love J, Wehrli FW (2011) Quantifying cortical bone water in vivo by three-dimensional ultra-short echo-time MRI. NMR Biomed 24(7):855–864
24. Jang H, Liu F, Bradshaw T, McMillan AB (2018) Rapid dual-echo ramped hybrid encoding MR-based attenuation correction (d RHE-MRAC) for PET/MR. Magn Reson Med 79(6):2912–2922
25. Jang H, Liu F, Zhao G, Bradshaw T, McMillan AB (2018) Deep learning based MRAC using rapid ultrashort echo time imaging. Med Phys 45(8):3697–3704
26. Juttukonda MR, Mersereau BG, Chen Y, Su Y, Rubin BG, Benzinger TL, Lalush DS, An H (2015) MR-based attenuation correction for PET/MRI neurological studies with continuous-valued attenuation coefficients for bone through a conversion from R2* to CT-Hounsfield units. Neuroimage 112:160–168
27. Ribeiro AS, Kops ER, Herzog H, Almeida P (2013) Skull segmentation of UTE MR images by probabilistic neural network for attenuation correction in PET/MR. Nucl Instrum Methods Phys Res Sect A 702:114–116
28. Aitken A, Giese D, Tsoumpas C, Schleyer P, Kozerke S, Prieto C, Schaeffter T (2014) Improved UTE-based attenuation correction for cranial PET-MR using dynamic magnetic field monitoring. Med Phys 41:1

29. Grodzki DM, Jakob PM, Heismann B (2012) Ultrashort echo time imaging using pointwise encoding time reduction with radial acquisition (PETRA). Magn Reson Med 67(2):510–518
30. Kobayashi N, Goerke U, Wang L, Ellermann J, Metzger GJ, Garwood M (2015) Gradient-modulated PETRA MRI. Tomography 1(2):85
31. Aida N, Niwa T, Fujii Y, Nozawa K, Enokizono M, Murata K, Obata T (2016) Quiet T1-weighted pointwise encoding time reduction with radial acquisition for assessing myelination in the pediatric brain. Am J Neuroradiol 37(8):1528–1534
32. Grodzki DM, Heismann B (2013) Quiet T1-weighted head scanning using PETRA. In: Proceedings of the 21st Annual Meeting of ISRMRM
33. Ida M, Wakayama T, Nielsen ML, Abe T, Grodzki DM (2015) Quiet T1-weighted imaging using PETRA: Initial clinical evaluation in intracranial tumor patients. J Magn Reson Imaging 41(2):447–453
34. Garwood M (2013) MRI of fast-relaxing spins. J Magn Reson 229:49–54
35. Sharafi A, Baboli R, Chang G, Regatte RR (2019) 3D–T1ρ prepared zero echo time-based PETRA sequence for in vivo biexponential relaxation mapping of semisolid short-T2 tissues at 3 T. J Magn Reson Imaging 50:1207–1218
36. Doran SJ, Charles-Edwards L, Reinsberg SA, Leach MO (2005) A complete distortion correction for MR images: I. Gradient warp correction. Phys Med Biol 50(7):1343
37. Huang KC, Cao Y, Baharom U, Balter JM (2016) Phantom-based characterization of distortion on a magnetic resonance imaging simulator for radiation oncology. Phys Med Biol 61(2):774
38. Pappas E, Seimenis I, Moutsatsos A, Georgiou E, Nomikos P, Karaiskos P (2016) Characterization of system-related geometric distortions in MR images employed in Gamma Knife radiosurgery applications. Phys Med Biol 61(19):6993
39. Pappas EP, Alshanqity M, Moutsatsos A, Lababidi H, Alsafi K, Georgiou K, Karaiskos P, Georgiou E (2017) MRI-related geometric distortions in stereotactic radiotherapy treatment planning: evaluation and dosimetric impact. Technol Cancer Res Treatment 16(6):1120–1129
40. Wang D, Doddrell DM, Cowin G (2004) A novel phantom and method for comprehensive 3-dimensional measurement and correction of geometric distortion in magnetic resonance imaging. Magn Reson Imaging 22(4):529–542
41. Wang H, Balter J, Cao Y (2013) Patient-induced susceptibility effect on geometric distortion of clinical brain MRI for radiation treatment planning on a 3T scanner. Phys Med Biol 58(3):465
42. Atkinson IC, Lu A, Thulborn KR (2009) Characterization and correction of system delays and eddy currents for MR imaging with ultrashort echo-time and time-varying gradients. Magn Reson Med 62(2):532–537
43. Law M, Yuan J, Wong O, Yu S (2016) SU-G-IeP1-08: MR geometric distortion dependency on imaging sequence, acquisition orientation and receiver bandwidth of a dedicated 1.5 T MR-simulator. Med Phys 43(6 Part 25):3646–3646
44. Baldwin LN, Wachowicz K, Fallone BG (2009) A two-step scheme for distortion rectification of magnetic resonance images. Med Phys 36(9 Part 1):3917–3926
45. Seibert T, White N, Kim G, McDonald C, Farid N, Moiseenko V, Bartsch H, Kuperman J, Holland D, Mundt A (2014) Distortion inherent to magnetic resonance imaging (MRI) can lead to geometric miss in radiosurgery planning. Int J Radiat Oncol Biol Phys 90(1):S97
46. Liney G, Owen S, Beaumont A, Lazar V, Manton D, Beavis A (2013) Commissioning of a new wide-bore MRI scanner for radiotherapy planning of head and neck cancer. Br J Radiol 86(1027):20130150
47. Liney GP, Moerland MA (2014) Magnetic resonance imaging acquisition techniques for radiotherapy planning. Semin Radiat Oncol 24(3):160–168
48. Bernstein MA, Zhou XJ, Polzin JA, King KF, Ganin A, Pelc NJ, Glover GH (1998) Concomitant gradient terms in phase contrast MR: analysis and correction. Magn Reson Med 39(2):300–308
49. Huang SY, Seethamraju RT, Patel P, Hahn PF, Kirsch JE, Guimaraes AR (2015) Body MR imaging: artifacts, k-Space, and solutions. Radiographics 35(5):1439–1460
50. Constantinides C (2016) Magnetic resonance imaging: the basics. CRC Press Taylor & Francis, Boca Raton
51. Spees WM, Buhl N, Sun P, Ackerman JJ, Neil JJ, Garbow JR (2011) Quantification and compensation of eddy-current-induced magnetic-field gradients. J Magn Reson 212(1):116–123
52. Jang H, McMillan AB (2017) A rapid and robust gradient measurement technique using dynamic single-point imaging. Magn Reson Med 78(3):950–962
53. Vannesjo SJ, Graedel NN, Kasper L, Gross S, Busch J, Haeberlin M, Barmet C, Pruessmann KP (2016) Image reconstruction using a gradient impulse response model for trajectory prediction. Magn Reson Med 76(1):45–58
54. Vannesjo SJ, Haeberlin M, Kasper L, Pavan M, Wilm BJ, Barmet C, Pruessmann KP (2013) Gradient system characterization by impulse response measurements with a dynamic field camera. Magn Reson Med 69(2):583–593
55. Tyler DJ, Robson MD, Henkelman RM, Young IR, Bydder GM (2007) Magnetic resonance imaging with ultrashort TE (UTE) PULSE sequences: technical considerations. J Magn Reson Imaging 25(2):279–289
56. Du YP, Joe Zhou X, Bernstein MA (2002) Correction of concomitant magnetic field-induced image artifacts in nonaxial echo-planar imaging. Magn Reson Med 48(3):509–515
57. Nieminen JO, Ilmoniemi RJ (2010) Solving the problem of concomitant gradients in ultra-low-field MRI. J Magn Reson 207(2):213–219
58. King KF, Ganin A, Zhou XJ, Bernstein MA (1999) Concomitant gradient field effects in spiral scans. Magn Reson Med 41(1):103–112
59. Tao S, Weavers PT, Trzasko JD, Huston J III, Shu Y, Gray EM, Foo TK, Bernstein MA (2018) The effect of concomitant fields in fast spin echo acquisition on asymmetric MRI gradient systems. Magn Reson Med 79(3):1354–1364
60. Zhou XJ, Tan SG, Bernstein MA (1998) Artifacts induced by concomitant magnetic field in fast spin-echo imaging. Magn Reson Med 40(4):582–591
61. Zhou XJ, Du YP, Bernstein MA, Reynolds HG, Maier JK, Polzin JA (1998) Concomitant magnetic-field-induced artifacts in axial echo planar imaging. Magn Reson Med 39(4):596–605
62. Balcom BJ, MacGregor RP, Beyea S, Green D, Armstrong R, Bremner T (1996) Single-point ramped imaging with t1enhancement (SPRITE). J Magn Reson 123:131–134
63. Özen AC (2017) Novel MRI technologies for structural and functional imaging of tissues with ultra-short T2 values. KIT Scientific Publishing, Karlsruhe, p 34
64. Gustafsson C, Nordström F, Persson E, Brynolfsson J, Olsson L (2017) Assessment of dosimetric impact of system specific geometric distortion in an MRI only based radiotherapy workflow for prostate. Phys Med Biol 62(8):2976
65. Atherton TJ, Kerbyson DJ (1999) Size invariant circle detection. Image Vis Comput 17(11):795–803
66. Myronenko A, Song X (2010) Point set registration: coherent point drift. IEEE Trans Pattern Anal Mach Intell 32(12):2262–2275
67. Myronenko A, Song X, Carreira-Perpinán MA (2007) Non-rigid point set registration: coherent point drift. Proc Adv Neural Inf Proces Syst 2007:1009–1016

68. Johnstone E, Wyatt JJ, Henry AM, Short SC, Sebag-Montefiore D, Murray L, Kelly CG, McCallum HM, Speight R (2017) Systematic review of synthetic computed tomography generation methodologies for use in magnetic resonance imaging–only radiation therapy. Int J Radiat Oncol Biol Phys 100(1):199–217
69. Paulson ES, Erickson B, Schultz C, Allen Li X (2015) Comprehensive MRI simulation methodology using a dedicated MRI scanner in radiation oncology for external beam radiation treatment planning. Med Phys 42(1):28–39
70. Herrmann K-H, Krämer M, Reichenbach JR (2016) Time efficient 3D radial UTE sampling with fully automatic delay compensation on a clinical 3T MR scanner. PLoS ONE 11:3
71. Grodzki DM, Jakob PM, Heismann B (2012) Correcting slice selectivity in hard pulse sequences. J Magn Reson 214:61–67
72. Zhao X (2019) Mri-based assessment of cortical bone matrix and mineral properties in a clinical setting. Publicly Accessible Penn Dissertations, 3464. https://repository.upenn.edu/edissertations/3464